

Tailoring spontaneous symmetry breaking in engineered van der Waals superlattices

Keda Jin,^{1,2,3,*} Lennart Klebl,⁴ Zachary A. H. Goodwin,^{5,6} Junting Zhao,^{1,2,3} Felix Lüpke,^{1,2,7} Dante M. Kennes,^{8,2,9} Jose Martinez-Castro,^{1,2,3} and Markus Ternes^{1,2,3,†}

¹*Peter Grünberg Institut (PGI-3), Forschungszentrum Jülich, 52425 Jülich, Germany*

²*Jülich Aachen Research Alliance, Fundamentals of Future Information Technology, 52425 Jülich, Germany*

³*Institut für Experimentalphysik II B, RWTH Aachen, 52074 Aachen, Germany*

⁴*Institut für Theoretische Physik und Astrophysik and Würzburg-Dresden Cluster of Excellence ctd.qmat, Universität Würzburg, 97074 Würzburg, Germany*

⁵*Department of Materials, University of Oxford, Parks Road, Oxford OX1 3PH, United Kingdom*

⁶*John A Paulson School of Engineering and Applied Sciences, Harvard University, Cambridge, MA, USA*

⁷*Institute of Physics II, Universität zu Köln, Zùlpicher Straße 77, 50937 Köln, Germany*

⁸*Institut für Theorie der statistischen Physik, RWTH Aachen, 52074 Aachen*

⁹*Max Planck Institute for the Structure and Dynamics of Matter, Center for Free Electron Laser Science, 22761 Hamburg, Germany*

Abstract

Superlattice engineering in van der Waals heterostructures (e. g. by moiré engineering) provides a powerful platform for designing electronic bands and realising correlated and topological quantum phenomena. Here, we pioneer a scheme to tailor superpotentials based on intrinsic substrate electronic orders. We show that this establishes a robust, self-aligned, and highly versatile route to band-structure control as we demonstrate in graphene by engineering two distinct, nearly commensurate superlattices using the charge density waves of 1T-NbSe₂. In these superlattices the graphene's Dirac cones are folded either to the Γ -point or to the K-points of the mini-Brillouin zone. Using scanning tunnelling microscopy, we observe that the Γ -folded system preserves C_3 symmetry, while the K-folded system exhibits spontaneous symmetry breaking. Combining density functional theory with an interlayer interaction model, we reveal that this difference is not electronically driven but originates from a structural instability. Our work establishes superlattice engineering for designer quantum states and unveils a structural mechanism for controlled emergent symmetry breaking.

MAIN

Superlattices in van der Waals (vdW) heterostructures offer a way to reshape the electronic structure of two-dimensional (2D) materials and stabilise interaction-driven phases that are not present in the individual constituents [1–6]. By inducing a long-wavelength potential on top of the atomic lattice, one can induce band folding, reduce bandwidths, and strengthen electron-electron interactions [6–9]. A particularly successful implementation of this concept uses moiré patterns generated by twisting atomically thin layers [3, 10]. This strategy has led to the discovery of many novel phenomena, including correlated insulating states [3, 11], unconventional superconductivity [12–14], topological states [15, 16], the fractional quantum Hall effect [17, 18], and emergent magnetism [19, 20]. Notably, many of these phenomena involve spontaneous symmetry breaking, highlighting the connection between superlattice geometry and the emergence of new quantum phases.

An alternative approach to engineer superlattices is to use the intrinsic electronic order

* k.jin@fz-juelich.de

† m.ternes@fz-juelich.de

in one material, such as charge density waves (CDWs), to impose a superlattice potential in an adjacent layer through proximity effects [21–23]. Unlike moiré engineering via twist angles, where achieving the desired twist angle during fabrication can be challenging, superlattices based on intrinsic order offer an inherent advantage: when the two constituent lattices are nearly commensurate, the system spontaneously relaxes into an energetically favourable registry [24–26]. This ‘lock-in’ mechanism, in which the layers self-align through slight rotations or lateral sliding, yields structures that are both energetically stable and experimentally reproducible. As a result, this type of superlattice engineering provides a robust and deterministic platform for realising novel quantum phases.

In graphene, the symmetry of the superlattice defines at which points the Dirac cones appear in the mini-Brillouin zone (mBZ) [27]. As the K and K’ valleys of graphene are related by time-reversal symmetry, there are only two distinct folding configurations. In one configuration, both K and K’ valleys are folded onto the Γ point of the mBZ (Γ -folding), merging the two Dirac cones in momentum space [28, 29]. In the other configuration, the valley identities are retained, with K and K’ mapped separately to the K_m and K'_m corners of the mBZ (K-folding) [27, 30].

While symmetry arguments predict these two folding scenarios, they do not completely determine the resulting electronic structure. Hybridisation with substrate bands, interlayer relaxation, and subtle variations in local stacking registry may profoundly reshape the band structure in ways that cannot be anticipated from geometry alone [25, 31]. Moreover, such effects may differ qualitatively between the two configurations: do Γ -folding and K-folding produce equivalent electronic reconstructions, or does one geometry harbour instabilities absent in the other? Answering this question requires the combination of experiment and theory within a controlled material system.

Here, we demonstrate deterministic control over the Dirac cone folding by using the CDW in 1T-NbSe₂ [32–34] to engineer two distinct, nearly commensurate superlattices on a graphene layer. We create a 2×2 superlattice relative to the CDW lattice that exhibits Γ -folding, and a $\sqrt{3} \times \sqrt{3}$ R30° superlattice that exhibits K-folding. Using scanning tunnelling microscopy and spectroscopy (STM/STS), we show that the Γ -folded system preserves all underlying symmetries, while the K-folded system exhibits a spontaneous breaking of the C_3 symmetry. This symmetry breaking is not electronically driven but originates from variations in the local stacking registry between graphene and NbSe₂, which modulate the

interlayer hybridisation.

Through mechanical stacking with carefully selected rotation angles θ , we create near-commensurate alignments between the $\sqrt{13} \times \sqrt{13}$ R13.9° CDW in 1T-NbSe₂ and a monolayer of graphene (Fig. 1a and Methods). The condition for an exact commensurate superlattice is given by the linear Diophantine equation [35, 36]:

$$m\mathbf{R}(\theta)\mathbf{a}_{G1} + n\mathbf{R}(\theta)\mathbf{a}_{G2} = j\mathbf{a}_{CDW1} + k\mathbf{a}_{CDW2}, \quad (1)$$

with \mathbf{a}_{G1} and \mathbf{a}_{G2} as the primitive lattice vectors of graphene, \mathbf{a}_{CDW1} and \mathbf{a}_{CDW2} as those of the CDW in 1T-NbSe₂, and $\mathbf{R}(\theta)$ as the rotation of the graphene lattice with respect to the CDW by an angle θ . The integers m, n, j , and k define the commensurate condition.

However, the different periodicities of the 1T-NbSe₂ CDW and the graphene lattice mean that equation 1 has no integer solution. This geometric incommensurability motivates a mismatch function that quantifies how closely the two lattices can approach commensurability:

$$f(\theta) = \min_{m,n \in \mathbb{Z}} |m\mathbf{R}(\theta)\mathbf{a}_{G1} + n\mathbf{R}(\theta)\mathbf{a}_{G2} - j\mathbf{a}_{CDW1} - k\mathbf{a}_{CDW2}|. \quad (2)$$

This function computes the minimal distance between any rotated graphene lattice vector (spanned by the integers m and n , and the rotation angle θ) and the target CDW superlattice vector. The results for a 2×2 superlattice (with $j = 2$ and $k = 0$) and a $\sqrt{3} \times \sqrt{3}$ R30° superlattice (with $j = k = 1$) are shown in Fig. 1b (for additional solutions see Suppl. Mat. 1). These two geometries are of particular interest, because they produce the two distinct band-folding scenarios: the 2×2 superlattice, whose stacking configuration is shown in Fig. 1c,d exhibits Γ -folding, while the $\sqrt{3} \times \sqrt{3}$ R30° superlattice (stacking configuration in Fig. 1e,f) shows K-folding, preserving valley identity.

Figures 1g-j show atomically resolved STM topographies and the corresponding fast Fourier transformations (FFTs) of two samples with chosen θ close to those for near-commensurate 2×2 and $\sqrt{3} \times \sqrt{3}$ R30° superlattices. Both topographic images reveal a strong periodic height modulation of the graphene layer, imprinted by the underlying triangular CDW lattice of the 1T-NbSe₂. The CDW maxima, which correspond to the centres of the Star-of-David clusters characteristic of the 1T phase, appear bright in the topography. Following the procedure described in Ref. [38], we extract from the FFTs a very small heterostrain $\varepsilon < 0.5\%$ in both samples (Suppl. Mat. 2). Despite their similarities, the topographies of the two samples differ in a revealing way. In the 2×2 superlattice,

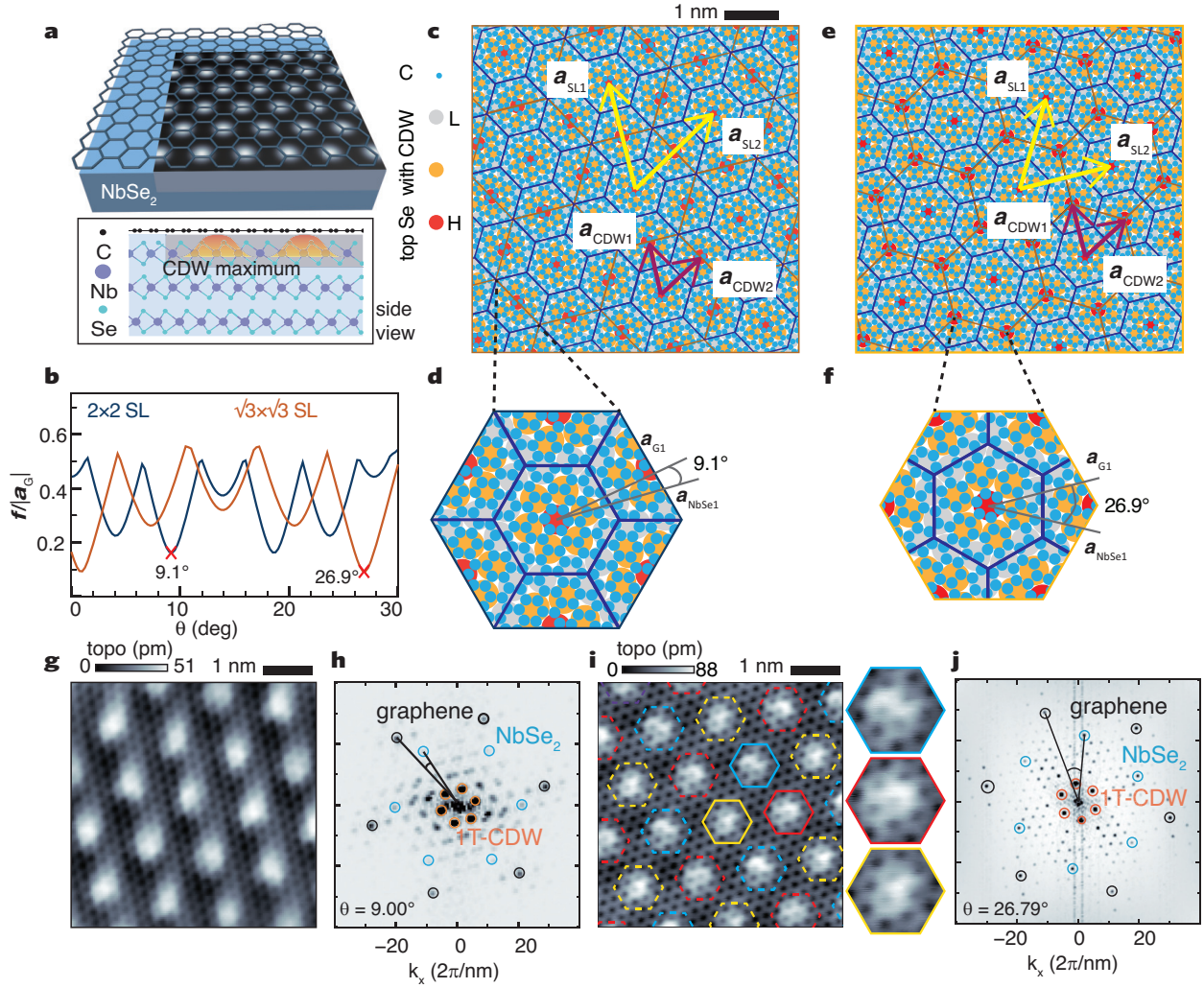


FIG. 1. **Superlattice Engineering.** **a**, Scheme of the graphene on 1T-NbSe₂/2H-NbSe₂ van der Waals heterostructure. The side view illustrates the charge density wave (CDW) maxima. **b**, Twist-angle θ dependent mismatch between the graphene lattice and the 2×2 (blue) and $\sqrt{3} \times \sqrt{3}$ R30° (orange) superlattice of the 1T-CDW in units of the graphene lattice constant. Here, we use the Wood's notation $\sqrt{3} \times \sqrt{3}$ R30° to denote a superlattice with unit vectors $\sqrt{3}$ times larger than those of the CDW lattice, rotated by 30° [37]. **c**, Scheme of the stacking configuration of a 2×2 commensurate superlattice realised by compressing the graphene lattice by a heterostrain of $\varepsilon = 4.1\%$. **d**, Zoom-in of the supercell. **e**, **f**, Same as (c, d) but for a $\sqrt{3} \times \sqrt{3}$ R30° commensurate superlattice with $\varepsilon = 1.8\%$. **g**, **h**, Atomically resolved STM topography and its FFT with $\theta = 9.0^\circ$ and $\varepsilon = 0.3\%$ ($V = 0.5$ V, $I = 200$ pA). **i**, **j**, Same as (g, h) for the sample with $\theta = 26.8^\circ$ and $\varepsilon = 0.4\%$ ($V = 0.3$ V, $I = 60$ pA). Colored hexagons mark the 3 different CDW maxima which repeat periodically, building up the $\sqrt{3} \times \sqrt{3}$ R30° supercell.

all CDW maxima show a nearly identical local contrast (Fig. 1g), whereas three distinct stacking configurations that repeat periodically across the surface can be identified in the $\sqrt{3} \times \sqrt{3}$ R30° system (Fig. 1i). This suggests that in the $\sqrt{3} \times \sqrt{3}$ R30° superlattice, the precise location of the carbon atoms with respect to the CDW lattice has a stronger influence on the interactions between the two layers than in the 2×2 superlattice. As we will discuss below, this difference affects the electronic structure and the symmetries of the two samples.

We begin by examining the 2×2 superlattice using differential conductance (dI/dV) spectroscopy, whose intensity is proportional to the local density of states (LDOS). Figure 2a shows dI/dV spectra acquired along a line, starting at the centre of the CDW maximum (referred to as A-site), and moving towards the midpoint between two neighbouring clusters (B-site). At the A-site, the dI/dV spectrum exhibits three pronounced peaks at energies E_{L1} , E_{L2} , and E_{L3} (see Suppl. Mat. 3 and 4). These peaks are absent in measurements taken at 1T/2H-NbSe₂ or graphene/2H-NbSe₂ heterostructures (Fig. 2b), confirming that they arise specifically from the interaction between the graphene sheet and the 1T-NbSe₂ layer.

As the tip moves from the A- to the B-site, the peaks decay in intensity, while a new feature at E_{v1} emerges with maximum intensity at the B-site. These complementary behaviours are visualised directly in constant energy dI/dV maps. At E_{L1} and E_{L2} , the dI/dV maps exhibit a dot-like structure with high intensity at the A-sites (Fig. 2c,d). The FFTs of these maps reveal significant intensity exclusively at the Bragg peaks corresponding to the reciprocal vectors of the CDW, $\mathbf{Q}_i^{\text{CDW}}$, suggesting that the spatial variation of the dI/dV can be described by a Fourier series expansion over these wavevectors as:

$$dI/dV(\mathbf{r}, V) = A_0(V) + \sum_{i=1}^3 A_i(V) \cos(\mathbf{Q}_i^{\text{CDW}} \cdot \mathbf{r} + \varphi_i(V)). \quad (3)$$

In this equation, $A_{1,2,3}$ are the amplitudes and $\varphi_{1,2,3}$ the phase-shifts of the LDOS modulation along the three fundamental directions of the CDW [39] (see Suppl. Mat. 5). The phases $\varphi_i(V)$ define the real-space registry of the LDOS modulation relative to the CDW superlattice. When $\varphi_i = 0$, the dI/dV maxima align with the A-sites, producing the dot-like pattern as seen at L_1 and L_2 . Near $V \approx 1$ V, all three phases simultaneously undergo a π -shift, resulting in an inversion of the LDOS contrast and a transformation of the dot-like pattern into a honeycomb-like structure (Fig. 2e). At the energy of L_3 , the phases adopt

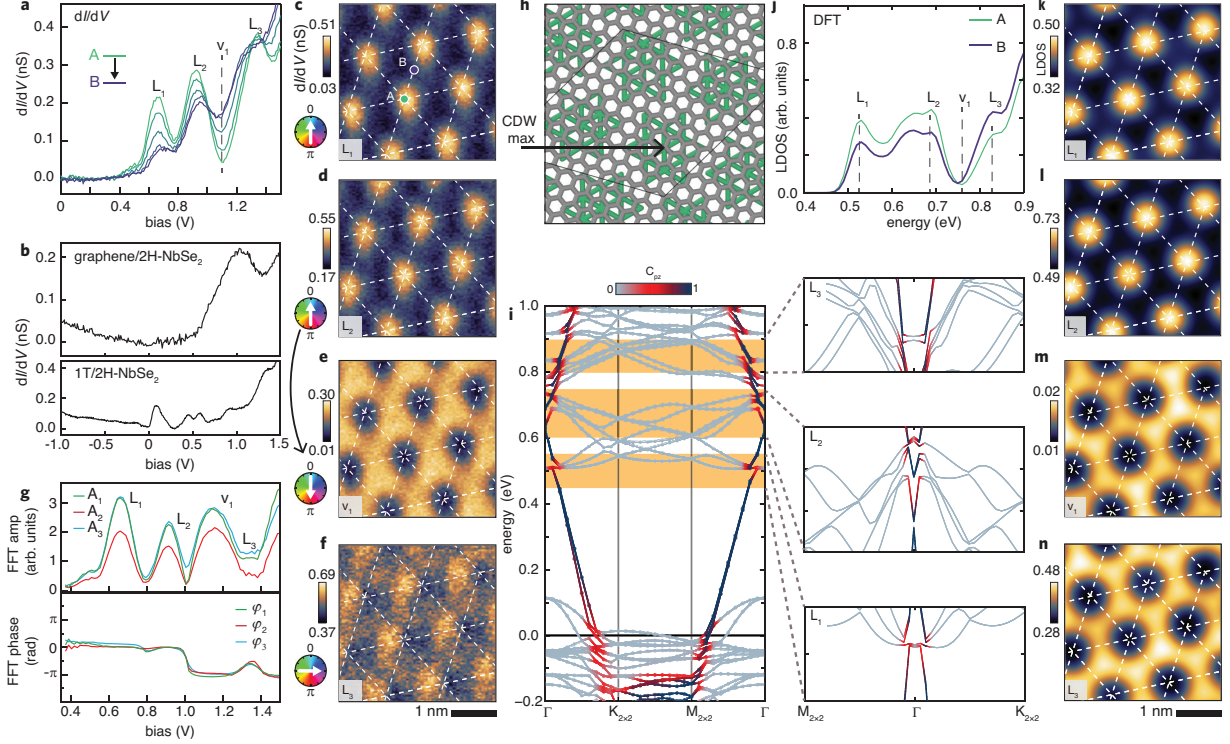


FIG. 2. **Electronic structure of the 2×2 superlattice.** **a**, Spectra measured between the A- and B-sites, marked in panel c, show three peaks at energies $E_{L1} = (0.66 \pm 0.01)$ eV, $E_{L2} = (0.92 \pm 0.01)$ eV, and $E_{L3} = (1.36 \pm 0.01)$ eV and a dip at $E_{v1} = (1.10 \pm 0.01)$ eV. **b**, On graphene/2H-NbSe₂ and 1T-NbSe₂/2H-NbSe₂ these features are absent. **c-f**, dI/dV maps measured at biases corresponding to E_{L1-L3} , and E_{v1} . **g**, Evolution of the FFT amplitudes A_{1-3} (top) and phases φ_{1-3} (bottom) extracted from the dI/dV maps. **h**, Schematic Model used for the DFT calculations. **i**, Calculated band structure of the superlattice mBZ and zoom-ins to the bands near the L_{1-3} states. The hybridised states are coded in red. **j**, Calculated LDOS at the A- and B-sites. **k-n**, Calculated LDOS maps at energies corresponding to the L_{1-3} , and v_1 features.

intermediate values, $\varphi_{1-3} \approx -\pi/2$, shifting the intensity maxima to positions between the A- and B-sites (Fig. 2f). A significant finding of this analysis is that A_{1-3} and φ_{1-3} evolve similarly across the measured energy range (Fig. 2g), indicating the preservation of the underlying C_3 rotational symmetry of the CDW lattice. The small difference in relative intensity might originate from a slight directional dependence of the probing tip.

To understand the origin of the observed spectral features, we performed DFT calculations (see Methods) for a commensurate 2×2 superlattice (Fig. 2h). The superlattice

potential defines the mBZ into which the original bands are folded (Fig. 2i). The key feature of this geometry is the Γ -folding: the Dirac cones from both the K and K' valleys of pristine graphene fold onto the Γ point of the mBZ. This valley degeneracy, combined with hybridisation with the NbSe₂ bands, produces peaks in the calculated LDOS (Fig. 2j) and the corresponding LDOS maps (Fig. 2k-n), which qualitatively reproduce the experimental observations.

We now turn to the electronic structure of the $\sqrt{3} \times \sqrt{3}$ R30° superlattice. At the A-site, we observe spectral features that are similar to those in the 2×2 superlattice, albeit with a subtle shift of the peak positions (Fig. 3a). The three B-sites, which are related by a 120° rotation around the A-site, however, are electronically inequivalent: The B₁-site shows an additional peak (L'_1) and increased intensity at L_1 , but decreased intensity at L_2 , compared to the B₂- and B₃-sites (Fig. 3b). Applying the same FFT phase analysis to this superlattice reveals a much more complex behaviour (Fig. 3c): At the energy of peak L_1 , we observe a dot-like pattern, accompanied by stripes along one direction (Fig. 3d), resulting in amplitudes $A_1 \approx A_3 \ll A_2$ and nearly aligned phases ($\varphi_{1-3} \approx 0$), providing a clear evidence of broken C_3 symmetry. As the energy increases to L_2 , the C_3 symmetry is restored, yielding a lattice of symmetric circular dots at A-sites (Fig. 3e).

Between L_2 and v_1 , we again observe a transition from a dot-like to a honeycomb-like LDOS pattern, but, unlike the symmetry-preserving transition in the 2×2 system, this transition proceeds through a series of staggered phase jumps that progressively break C_3 symmetry (Fig. 3c). The first phase jump distorts the dots into ellipses along one axis (Fig. 3f); the second phase jump creates a transient stripe pattern (Fig. 3g); and the third phase jump completes the transformation to the honeycomb pattern (Fig. 3h). However, even at v_1 , the amplitudes remain unequal, with A_2 being dominant, confirming the persistence of the broken symmetry.

DFT calculations on this supercell confirm the K-folding (Fig. 3i). Hybridisation with the 1T-NbSe₂ bands gives rise to a series of prominent peaks, and the calculated LDOS maps qualitatively reproduce the measured dI/dV maps (Fig. 3j-n). Notably, the same FFT phase analysis applied to the calculated maps reveals a comparable series of staggered phase jumps (Fig. 3o), yielding asymmetric intermediate states with broken C_3 symmetry (Fig. 3m).

Although the DFT calculations capture the broken symmetry in the $\sqrt{3} \times \sqrt{3}$ R30° su-

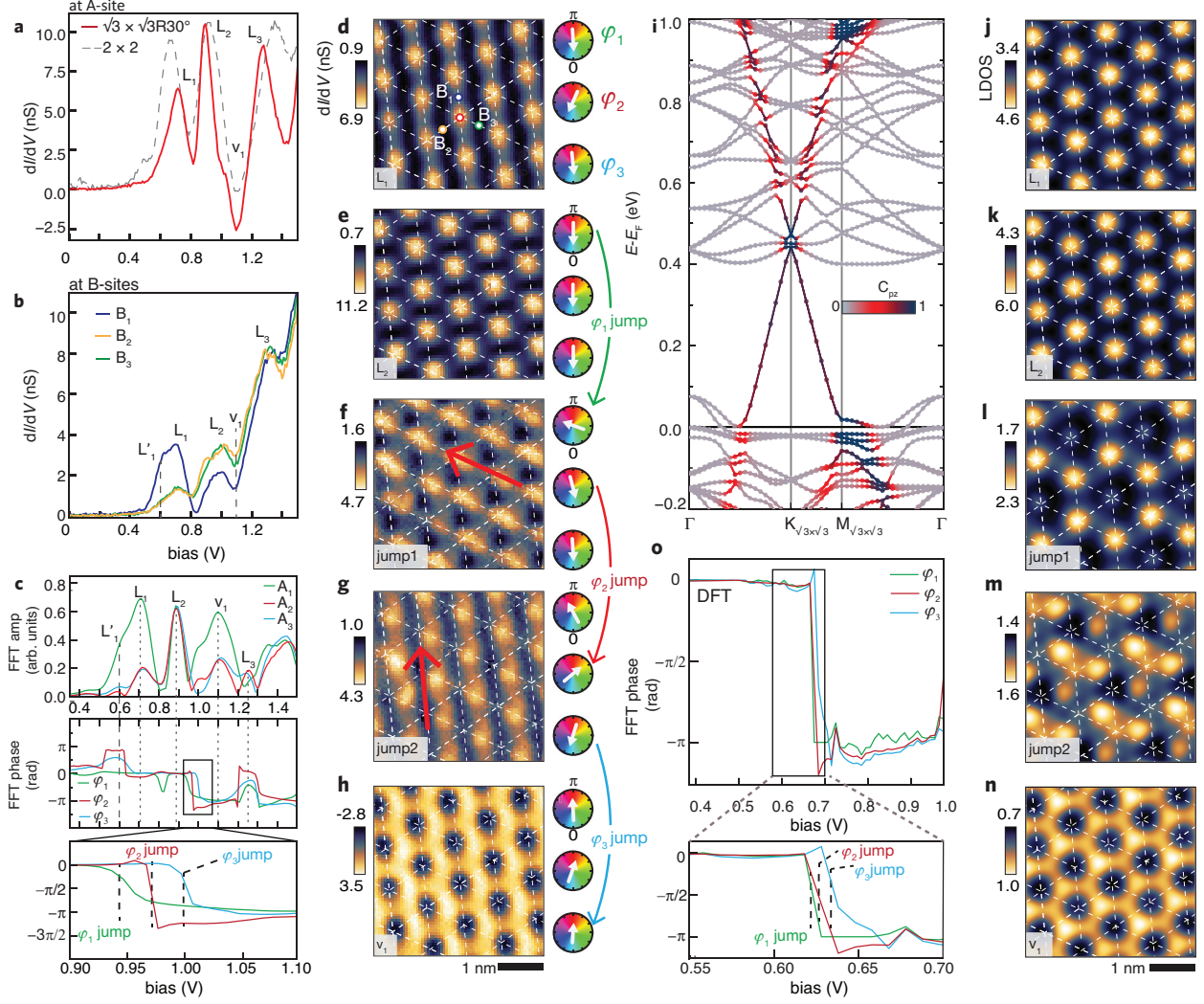


FIG. 3. **Electronic structure of the $\sqrt{3} \times \sqrt{3}$ R30° superlattice** **a**, Spectrum taken at the A-site (solid line) show peaks at energies $E_{L1} = 0.71 \pm 0.01$ eV, $E_{L2} = 0.90 \pm 0.01$ eV, and $E_{L3} = 1.27 \pm 0.01$ eV and a dip at $E_{V1} = 1.10 \pm 0.01$ eV. The spectrum measured in the 2×2 superlattice (dashed line, $\times 25$) is shown for comparison. **b**, Spectra recorded at the CDW minima B_1 (blue), B_2 (orange) and B_3 (green), which are rotated around the CDW maximum by 120° with respect to each other. At B_1 an additional peak L'_1 appears at $E_{L1'} = 0.62 \pm 0.01$ eV. **c**, Phase and amplitude from the FFT analysis of the dI/dV data as a function of bias. **d-h**, dI/dV maps at the indicated energies. **i**, Calculated band structure of the $\sqrt{3} \times \sqrt{3}$ R30° superlattice mini-Brillouin zone. **j-n**, DFT calculated LDOS maps, at the corresponding states. **o**, Similar phase analysis using the DFT-calculated LDOS data.

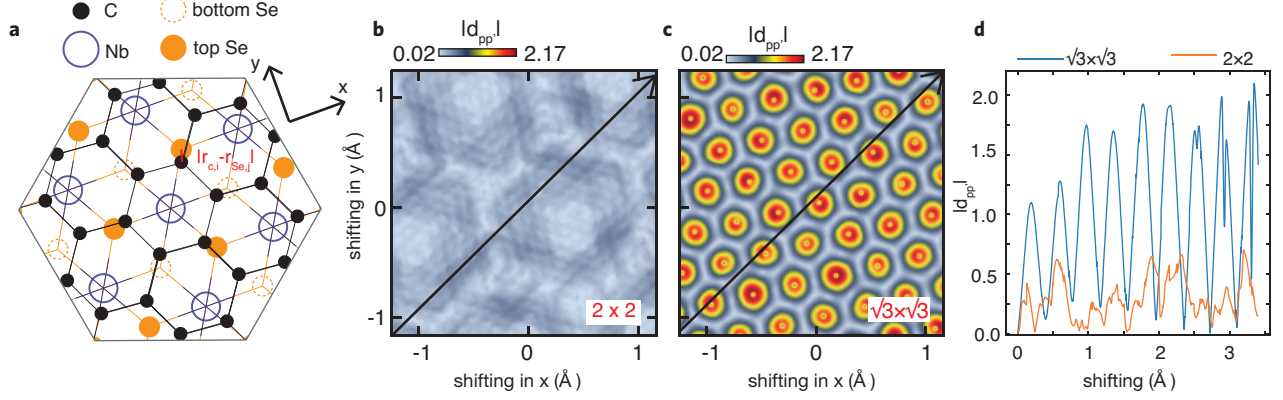


FIG. 4. **Geometric origin of the symmetry breaking.** **a**, Schematic of the interlayer interaction model. **b**, 2D resolved sliding map of the calculated hybridisation magnitude $|d_{pp}|$ for the 2×2 superlattice with sliding directions defined in **a**. **c**, 2D resolved sliding map of the $|d_{pp}|$ for the $\sqrt{3} \times \sqrt{3}$ R30° superlattice. **d**, Comparison of the $|d_{pp}|$ as a function of sliding between these two commensurate configurations, along the sliding paths indicated in **b** and **c**.

perlattice and its absence in the 2×2 superlattice, the microscopic origin of this symmetry breaking remains unclear within DFT. To elucidate the mechanism, we developed a simplified atomistic model that quantifies the spatial average of the interlayer coupling based on local atomic registry. This model enables us to simulate the influence of lateral sliding of the graphene layer with respect to the NbSe₂ and the influence of isotropic strain on the interlayer hybridisation.

Our model quantifies the net directional preference of hybridisation between the p_z orbitals of the carbon atoms in the graphene layer and the p orbitals of the topmost Se atoms in the NbSe₂ layer (Fig. 4a):

$$\mathbf{d}_{pp} = \sum_{i,j} \frac{\mathbf{r}_{C,i} - \mathbf{r}_{Se,j}}{|\mathbf{r}_{C,i} - \mathbf{r}_{Se,j}|} w(|\mathbf{r}_{C,i} - \mathbf{r}_{Se,j}|), \quad (4)$$

where the sum runs over all C atoms of the graphene and all Se atoms in the topmost NbSe₂ layer and $\mathbf{r}_{C,i}$ ($\mathbf{r}_{Se,j}$) denotes the position of the i -th carbon (j -th selenium) atom. The exponential weighting function $w(r) = e^{-\alpha r}$ represents the distance dependence of Slater-Koster tight-binding parameters arising from orbital overlap [40]. The decay constant $\alpha = 0.3 \text{ \AA}^{-1}$ ensures that nearest-neighbour C–Se pairs dominate the hybridisation. Further details are provided in Suppl. Mat. 6.

The results for laterally sliding graphene in the commensurate 2×2 and $\sqrt{3} \times \sqrt{3}$ R30°

superlattices are shown in Fig. 4b-d, and reveal a striking difference. In the 2×2 superlattice, d_{pp} remains nearly constant under sliding, indicating a flat hybridisation landscape that is insensitive to the local registry. In the $\sqrt{3} \times \sqrt{3}$ R30° superlattice, by contrast, the average hybridisation is strongly modulated. This behaviour persists when we allow for an incommensurate graphene lattice (Suppl. Mat. 7).

This different response enables us to address the origin of the symmetry breaking. In the $\sqrt{3} \times \sqrt{3}$ R30° geometry, the hybridisation landscape of the ideal structure is highly susceptible to perturbations; even a small lateral shift or strain can break the delicate balance of the three equivalent CDW directions and lift their degeneracy. The 2×2 geometry, with its smoother hybridisation landscape, is more robust against such perturbations and maintains C_3 symmetry even under realistic sample conditions. Therefore, the symmetry breaking observed in the $\sqrt{3} \times \sqrt{3}$ R30° superlattice arises from a geometric instability that is intrinsic to this superlattice configuration.

The superlattice engineering strategy demonstrated here can be naturally extended to a broad class of vdW heterostructures beyond our specific example. By selecting host materials with different CDW periodicities and symmetries, one can systematically design band-folding pathways and target specific points of the mBZ for Dirac cones or other band features. Promising candidates include graphene on 1T-TaS₂ [21], whose $\sqrt{13} \times \sqrt{13}$ R13.9° CDW has a slightly larger periodicity than that of 1T-NbSe₂, as well as other transition-metal dichalcogenides with commensurate or nearly commensurate CDWs. In such systems, the competition between different registries, coupled to the structural instabilities revealed in this work, is expected to generate a rich landscape of symmetry-broken ground states, including nematic and ferroic-like orders that could be tuned by strain, pressure, or electrostatic gating.

Our approach can be extended to semiconducting 2D crystals such as WSe₂ on 1T-NbSe₂ or 1T-TaS₂. In these heterostructures, CDW-induced superlattices provide a route to engineer not only electronic minibands but also excitonic dispersions, valley selection rules, and radiative lifetimes through zone folding of exciton states [41]. This opens opportunities to realise designer excitonic lattices, control interlayer and moiré-like excitons [42]. More broadly, combining CDW-based proximity superlattices with twist, strain, or multilayer stacking could enable hybrid CDW-moiré platforms in which structural relaxation, electronic correlations, and topology are all on comparable energy scales. Our results thus

establish CDW-mediated superlattice engineering as a robust and deterministic strategy for creating and controlling emergent quantum phases in vdW heterostructures, and motivate future experiments that exploit structural degrees of freedom as an equal partner to electronic interactions in the design of quantum materials.

METHODS

A. Sample fabrication

We fabricated the heterostructures in an Ar-filled glove box following a suspended dry pickup and flip-over assembly technique [43]. We then placed the assembled heterostructure on top of a 285 nm Si/SiO₂ chip on which we constructed contact and tip guidance electrodes [44] by electron beam lithography (Suppl. Mat. 8).

Initial STM topographies of the graphene/2H-NbSe₂ heterostructures resolve the graphene lattice, the underlying NbSe₂ lattice, and the resulting moiré superlattice, but show no signatures of the 3×3 charge-density-wave (CDW) order (Suppl. Mat. 9), consistent with previous reports [45]. To realise graphene on 1T-NbSe₂, we employ local bias pulsing with the STM tip on graphene/2H-NbSe₂ [46], which induces a controlled phase transition from the 2H to the 1T polytype in the NbSe₂ layer beneath the graphene (Suppl. Mat. 10).

B. STM and STS measurements

All measurements were performed in ultra-high vacuum ($\leq 1 \times 10^{-10}$ mbar) and at a base temperature of $T = 6$ K. As tip we used electrochemically etched tungsten tips, flashed in ultra-high vacuum to remove the oxide layer and contamination. Additionally, the tip was prepared in-situ by repeatedly indenting it into the deposited gold contacts until it showed a flat density of states. STS was performed using a standard lock-in technique at a modulation frequency of 877 Hz and modulation voltages $V_{\text{mod}} = 10$ mV.

C. DFT calculations

Density functional theory calculations were performed in a plane-wave pseudopotential framework. We first relaxed the $\sqrt{13} \times \sqrt{13}$ R13.9° CDW unit cell of 1T-NbSe₂ with fixed in-plane lattice parameters, and then constructed commensurate 2×2 and $\sqrt{3} \times \sqrt{3}$ R30° graphene/1T-NbSe₂ supercells by straining graphene homoaxially and twisting its lattice vectors. The graphene layer was initially placed ~ 5 Å above the Nb plane, and all atomic positions in the heterostructures were relaxed.

We used a generalized-gradient exchange–correlation functional with van der Waals cor-

rections, ultrasoft pseudopotentials, a vacuum spacing of 20 Å, and kinetic-energy cutoffs of 40/400 Ry for wavefunctions/charge density. Moderately dense k -point meshes were employed for self-consistent calculations and further refined for non-self-consistent band-structure, (projected) DOS and real-space LDOS calculations. The resulting electronic structures capture the key qualitative differences between the 2×2 and $\sqrt{3} \times \sqrt{3}$ R30° superlattices, including their distinct band folding and symmetry properties. More details can be found in the Suppl. Mat. 11.

DATA AVAILABILITY

All data presented in this study are available on the Jülich Data Repository at xxxxxxx

-
- [1] R. Bistritzer and A. H. MacDonald, Moiré bands in twisted double-layer graphene, *Proc. Natl. Acad. Sci. U.S.A* **108**, 12233 (2011).
 - [2] L. A. Ponomarenko, R. V. Gorbachev, G. L. Yu, D. C. Elias, R. Jalil, A. A. Patel, A. Mishchenko, A. S. Mayorov, C. R. Woods, J. R. Wallbank, M. Mucha-Kruczynski, B. A. Piot, M. Potemski, I. V. Grigorieva, K. S. Novoselov, F. Guinea, V. I. Fal’ko, and A. K. Geim, Cloning of Dirac fermions in graphene superlattices, *Nature* **497**, 594 (2013).
 - [3] Y. Cao, V. Fatemi, A. Demir, S. Fang, S. L. Tomarken, J. Y. Luo, J. D. Sanchez-Yamagishi, K. Watanabe, T. Taniguchi, E. Kaxiras, R. C. Ashoori, and P. Jarillo-Herrero, Correlated insulator behaviour at half-filling in magic-angle graphene superlattices, *Nature* **556**, 80 (2018).
 - [4] J. G. Checkelsky, B. A. Bernevig, P. Coleman, Q. Si, and S. Paschen, Flat bands, strange metals and the Kondo effect, *Nat. Rev. Mater.* **9**, 509 (2024).
 - [5] L. D. Du, Z. Huang, J. Zhang, F. Ye, Q. Dai, H. Deng, G. Zhang, and Z. Sun, Nonlinear physics of moiré superlattices, *Nat. Mater.* **23**, 1179 (2024).
 - [6] H. Zhang, J. Lu, K. Liu, Y. Wang, F. Wang, S. Wu, W. Chen, X. Cai, K. Watanabe, T. Taniguchi, J. Avila, P. Dudin, M. D. Watson, A. Louat, T. Sato, P. Yu, W. Duan, Z. Song, G. Chen, and S. Zhou, Moiré enhanced flat band in rhombohedral graphene, *Nat. Mater.* , 1 (2025).

- [7] H. Li, Z. Xiang, A. P. Reddy, T. Devakul, R. Sailus, R. Banerjee, T. Taniguchi, K. Watanabe, S. Tongay, A. Zettl, L. Fu, M. F. Crommie, and F. Wang, Wigner molecular crystals from multielectron moiré artificial atoms, *Science* **385**, 86 (2024).
- [8] Z. Zhang, J. Xie, W. Zhao, R. Qi, C. Sanborn, S. Wang, S. Kahn, K. Watanabe, T. Taniguchi, A. Zettl, M. Crommie, and F. Wang, Engineering correlated insulators in bilayer graphene with a remote Coulomb superlattice, *Nat. Mater.* **23**, 189 (2024).
- [9] K. P. Nuckolls and A. Yazdani, A microscopic perspective on moiré materials, *Nat. Rev. Mater.* **9**, 460 (2024).
- [10] Y. Guo, J. Pack, J. Swann, L. Holtzman, M. Cothrine, K. Watanabe, T. Taniguchi, D. G. Mandrus, K. Barmak, J. Hone, A. J. Millis, A. Pasupathy, and C. R. Dean, Superconductivity in 5.0° twisted bilayer WSe₂, *Nature* **637**, 839 (2025).
- [11] H. Tian, E. Codecido, D. Mao, K. Zhang, S. Che, K. Watanabe, T. Taniguchi, D. Smirnov, E.-A. Kim, M. Bockrath, and C. N. Lau, Dominant 1/3-filling correlated insulator states and orbital geometric frustration in twisted bilayer graphene, *Nat. Phys.* **20**, 1407 (2024).
- [12] Y. Cao, V. Fatemi, S. Fang, K. Watanabe, T. Taniguchi, E. Kaxiras, and P. Jarillo-Herrero, Unconventional superconductivity in magic-angle graphene superlattices, *Nature* **556**, 43 (2018).
- [13] L. Balents, C. R. Dean, D. K. Efetov, and A. F. Young, Superconductivity and strong correlations in moiré flat bands, *Nat. Phys.* **16**, 725 (2020).
- [14] M. Tanaka, J. I.-j. Wang, T. H. Dinh, D. Rodan-Legrain, S. Zaman, M. Hays, A. Almanakly, B. Kannan, D. K. Kim, B. M. Niedzielski, K. Serniak, M. E. Schwartz, K. Watanabe, T. Taniguchi, T. P. Orlando, S. Gustavsson, J. A. Grover, P. Jarillo-Herrero, and W. D. Oliver, Superfluid stiffness of magic-angle twisted bilayer graphene, *Nature* **638**, 99 (2025).
- [15] G. Chen, A. L. Sharpe, E. J. Fox, Y.-H. Zhang, S. Wang, L. Jiang, B. Lyu, H. Li, K. Watanabe, T. Taniguchi, Z. Shi, T. Senthil, D. Goldhaber-Gordon, Y. Zhang, and F. Wang, Tunable correlated Chern insulator and ferromagnetism in a moiré superlattice, *Nature* **579**, 56 (2020).
- [16] R. Su, D. Waters, B. Zhou, K. Watanabe, T. Taniguchi, Y.-H. Zhang, M. Yankowitz, and J. Folk, Moiré-driven topological electronic crystals in twisted graphene, *Nature* **637**, 1084 (2025).
- [17] Z. Lu, T. Han, Y. Yao, A. P. Reddy, J. Yang, J. Seo, K. Watanabe, T. Taniguchi, L. Fu, and L. Ju, Fractional quantum anomalous Hall effect in multilayer graphene, *Nature* **626**, 759 (2024).

- [18] K. P. Nuckolls, M. G. Scheer, D. Wong, M. Oh, R. L. Lee, J. Herzog-Arbeitman, K. Watanabe, T. Taniguchi, B. Lian, and A. Yazdani, Spectroscopy of the fractal Hofstadter energy spectrum, *Nature* **639**, 60 (2025).
- [19] A. L. Sharpe, E. J. Fox, A. W. Barnard, J. Finney, K. Watanabe, T. Taniguchi, M. A. Kastner, and D. Goldhaber-Gordon, Emergent ferromagnetism near three-quarters filling in twisted bilayer graphene, *Science* **365**, 605 (2019).
- [20] W. Zhao, B. Shen, Z. Tao, S. Kim, P. Knüppel, Z. Han, Y. Zhang, K. Watanabe, T. Taniguchi, D. Chowdhury, J. Shan, and K. F. Mak, Emergence of ferromagnetism at the onset of moiré kondo breakdown, *Nat. Phys.* **20**, 1772 (2024).
- [21] N. Tilak, M. Altvater, S.-H. Hung, C.-J. Won, G. Li, T. Kaleem, S.-W. Cheong, C.-H. Chung, H.-T. Jeng, and E. Y. Andrei, Proximity induced charge density wave in a graphene/1T-TaS₂ heterostructure, *Nat. Commun.* **15**, 8056 (2024).
- [22] B. Kim, J. Li, J. Park, H. Lim, G. Myeong, W. Shin, S. Kim, T. Jin, Q. Zhang, K. Sung, D. D. Le, K. Watanabe, T. Taniguchi, C.-H. Yang, E. Hwang, and S. Cho, Effect of charge density wave on the electronic transport in graphene, *ACS Appl. Electron. Mater.* **6**, 1174 (2024).
- [23] W.-M. Zhao, L. Zhu, Z. Nie, Q.-Y. Li, Q.-W. Wang, L.-G. Dou, J.-G. Hu, L. Xian, S. Meng, and S.-C. Li, Moiré enhanced charge density wave state in twisted 1T-TiTe₂/1T-TiSe₂ heterostructures, *Nat. Mater.* **21**, 284 (2022).
- [24] C. R. Woods, L. Britnell, A. Eckmann, R. S. Ma, J. C. Lu, H. M. Guo, X. Lin, G. L. Yu, Y. Cao, R. V. Gorbachev, A. V. Kretinin, J. Park, L. A. Ponomarenko, M. I. Katsnelson, Y. N. Gornostyrev, K. Watanabe, T. Taniguchi, C. Casiraghi, H.-J. Gao, A. K. Geim, and K. S. Novoselov, Commensurate-incommensurate transition in graphene on hexagonal boron nitride, *Nat. Phys.* **10**, 451 (2014).
- [25] H. Yoo, R. Engelke, S. Carr, S. Fang, K. Zhang, P. Cazeaux, S. H. Sung, R. Hovden, A. W. Tsen, T. Taniguchi, K. Watanabe, G.-C. Yi, M. Kim, M. Luskin, E. B. Tadmor, E. Kaxiras, and P. Kim, Atomic and electronic reconstruction at the van der Waals interface in twisted bilayer graphene, *Nat. Mater.* **18**, 448 (2019).
- [26] X. Lai, G. Li, A. M. Coe, J. H. Pixley, K. Watanabe, T. Taniguchi, and E. Y. Andrei, Moiré periodic and quasiperiodic crystals in heterostructures of twisted bilayer graphene on hexagonal boron nitride, *Nat. Mater.* **24**, 1019 (2025).

- [27] J. R. Wallbank, A. A. Patel, M. Mucha-Kruczyński, A. K. Geim, and V. I. Fal’ko, Generic miniband structure of graphene on a hexagonal substrate, *Phys. Rev. B* **87**, 245408 (2013).
- [28] C. Bao, H. Zhang, T. Zhang, X. Wu, L. Luo, S. Zhou, Q. Li, Y. Hou, W. Yao, L. Liu, P. Yu, J. Li, W. Duan, H. Yao, Y. Wang, and S. Zhou, Experimental Evidence of Chiral Symmetry Breaking in Kekulé-Ordered Graphene, *Phys. Rev. Lett.* **126**, 206804 (2021).
- [29] X. Qiu, T. Zhu, Z. Fan, K. Wang, Y. Mu, B. Yang, D. Wu, H. Zhang, C. Wang, H. Wang, and Y. Zhang, Giant Splitting of Folded Dirac Bands in Kekulé-ordered Graphene with Eu Intercalation, arXiv 10.48550/arxiv.2509.05633 (2025).
- [30] C. Ortix, L. Yang, and J. v. d. Brink, Graphene on incommensurate substrates: Trigonal warping and emerging Dirac cone replicas with halved group velocity, *Phys. Rev. B* **86**, 081405 (2011).
- [31] E. Barre, M. Dandu, S. Kundu, A. Sood, F. H. d. Jornada, and A. Raja, Engineering interlayer hybridization in van der Waals bilayers, *Nat. Rev. Mater.* **9**, 499 (2024).
- [32] M. Liu, J. Leveillee, S. Lu, J. Yu, H. Kim, C. Tian, Y. Shi, K. Lai, C. Zhang, F. Giustino, and C.-K. Shih, Monolayer 1T-NbSe₂ as a 2D-correlated magnetic insulator, *Sci. Adv.* **7**, eabi6339 (2021).
- [33] Y. Nakata, K. Sugawara, A. Chainani, H. Oka, C. Bao, S. Zhou, P.-Y. Chuang, C.-M. Cheng, T. Kawakami, Y. Saruta, T. Fukumura, S. Zhou, T. Takahashi, and T. Sato, Robust charge-density wave strengthened by electron correlations in monolayer 1T-TaSe₂ and 1T-NbSe₂, *Nat. Commun.* **12**, 5873 (2021).
- [34] X. Huang, J. L. Lado, J. Sainio, P. Liljeroth, and S. C. Ganguli, Doped Mott Phase and Charge Correlations in Monolayer 1T-NbSe₂, *Phys. Rev. Lett.* **134**, 046504 (2025).
- [35] D. T. S. Perkins, Symmetry preservation in commensurate twisted bilayers, *Phys. Rev. B* **112**, 035410 (2025).
- [36] P. Zeller and S. Günther, What are the possible moiré patterns of graphene on hexagonally packed surfaces? Universal solution for hexagonal coincidence lattices, derived by a geometric construction, *New J. Phys.* **16**, 083028 (2014).
- [37] E. A. Wood, Vocabulary of Surface Crystallography, *J. Appl. Phys.* **35**, 1306 (1964).
- [38] A. Kerelsky, L. J. McGilly, D. M. Kennes, L. Xian, M. Yankowitz, S. Chen, K. Watanabe, T. Taniguchi, J. Hone, C. Dean, A. Rubio, and A. N. Pasupathy, Maximized electron interactions at the magic angle in twisted bilayer graphene, *Nature* **572**, 95 (2019).

- [39] A. Pásztor, A. Scarfato, M. Spera, C. Barreateau, E. Giannini, and C. Renner, Holographic imaging of the complex charge density wave order parameter, *Phys. Rev. Res.* **1**, 033114 (2019).
- [40] J. C. Slater and G. F. Koster, Simplified LCAO method for the periodic potential problem, *Phys. Rev.* **94**, 1498 (1954).
- [41] M. Oudich, X. Kong, T. Zhang, C. Qiu, and Y. Jing, Engineered moiré photonic and phononic superlattices, *Nat. Mater.* **23**, 1169 (2024).
- [42] A. d. l. Torre, D. M. Kennes, E. Malic, and S. Kar, Advanced Characterization of the Spatial Variation of Moiré Heterostructures and Moiré Excitons, *Small* **21**, 2401474 (2025).
- [43] K. Jin, T. Wichmann, S. Wenzel, T. Samuely, O. Onufrienko, P. Szabó, K. Watanabe, T. Taniguchi, J. Yan, F. S. Tautz, F. Lüpke, M. Ternes, and J. Martinez-Castro, Assembly of Arbitrary Designer Heterostructures with Atomically Clean Interfaces, *Adv. Mater. Interfaces* **11**, 2300658 (2023).
- [44] J. Martinez-Castro, D. Mauro, A. Pásztor, I. Gutiérrez-Lezama, A. Scarfato, A. F. Morpurgo, and C. Renner, Scanning Tunneling Microscopy of an Air Sensitive Dichalcogenide Through an Encapsulating Layer, *Nano Lett.* **18**, 6696 (2018).
- [45] Y. Chen, L. Wu, H. Xu, C. Cong, S. Li, S. Feng, H. Zhang, C. Zou, J. Shang, S. A. Yang, K. P. Loh, W. Huang, and T. Yu, Visualizing the anomalous charge density wave states in graphene/NbSe₂ heterostructures, *Adv. Mater.* **32**, 2003746 (2020).
- [46] F. Bischoff, W. Auwärter, J. V. Barth, A. Schiffrin, M. Fuhrer, and B. Weber, Nanoscale phase engineering of niobium diselenide, *Chem. of Mater.* **29**, 9907 (2017).

ACKNOWLEDGMENTS

We would like to thank Tim Wehling, Tobias Wichmann and F. Stefan Tautz for their fruitful discussions and valuable feedback. We also gratefully acknowledge computing time granted through JARA on the supercomputer JURECA and the JURECA DC Evaluation platform at Forschungszentrum Jülich. Furthermore, the authors are grateful to the Helmholtz Nano Facility for its support regarding sample fabrication. K. J., F. L., D. M. K., J. M.-C., and M. T. acknowledge funding by the Deutsche Forschungsgemeinschaft (DFG, German Research Foundation) within the SPP 2244 (Projects 443416235, 422707584 and 443274199) and by a Major Instrumentation fund (INST 222/1296-1 FUGG). J. M.-C., and F. L. acknowledge funding from the Bavarian Ministry of Economic Affairs, Regional Development, and Energy within Bavaria’s High-Tech Agenda Project “Bausteine für das Quantencomputing auf Basis topologischer Materialien mit experimentellen und theoretischen Ansätzen”. J. M.-C. acknowledges funding from the Alexander von Humboldt Foundation. L. K. acknowledges support through the Würzburg-Dresden Cluster of Excellence on Complexity and Topology in Quantum Matter – ctd.qmat, Project-ID 390858490 – EXC 2147, and through the Research Unit QUAST, Project-ID 449872909 – FOR5249. M. T. acknowledges funding from the Heisenberg Program (TE 833/2) of the German Research Foundation. F. L. acknowledges financial support from Germany’s Excellence Strategy-Cluster of Excellence Matter and Light for Quantum Computing (ML4Q) through an Independence Grant. Z. A. H. G acknowledges support through the Glasstone Research Fellowship in Materials, University of Oxford.

Author contributions

K. J., J. M.-C., and M. T. conceived the project. K. J. fabricated the samples. K. J., J. Z. and J. M.-C. performed the STM experiments. K. J. and M. T. analyzed the data. L. K., Z. A. H. G., and D. M. K. performed the DFT and the geometry model calculations. F. L., D. M. K., J. M.-C., and M. T. supervised the project. K. J., and M. T. wrote the manuscript. All authors discussed and commented on the manuscript.

Competing financial interests

The authors declare no competing financial interests.